

# An intermittent detachment faulting system with a large sulfide deposit revealed by multi-scale magnetic surveys

**Tao Wu**

Second Institute of Oceanography, MNR

**Maurice Tivey**

Woods Hole Oceanographic Institution

**Chunhui Tao** (✉ [taochunhuimail@163.com](mailto:taochunhuimail@163.com))

Second Institute of Oceanography, MNR

**Jinhui Zhang**

Second Institute of Oceanography, MNR

**Fei Zhou**

Institute de Physique du Globe

**Yunlong Liu**

Second Institute of Oceanography, MNR <https://orcid.org/0000-0002-6215-6356>

---

## Article

**Keywords:** magmatic processes, tectonic processes, faulting system

**Posted Date:** December 30th, 2020

**DOI:** <https://doi.org/10.21203/rs.3.rs-127728/v1>

**License:** © ⓘ This work is licensed under a Creative Commons Attribution 4.0 International License.

[Read Full License](#)

---

**Version of Record:** A version of this preprint was published at Nature Communications on September 24th, 2021. See the published version at <https://doi.org/10.1038/s41467-021-25880-1>.

# Abstract

Magmatic and tectonic processes can contribute to discontinuous crustal accretion and play an important role in hydrothermal circulation at ultraslow-spreading ridges, however, it is difficult to accurately describe the processes without an age framework to constrain crustal evolution. Here we report on a multi-scale magnetic survey that provides constraints on the fine-scale evolution of a detachment faulting system that hosts hydrothermal activity at 49.7°E on the Southwest Indian Ridge. Reconstruction of the multi-stage detachment faulting history shows a previous episode of detachment faulting took place 0.76~1.48 My BP, while the present fault has been active for the past ~0.33 My just in the prime of life. This fault sustains hydrothermal circulation that has the potential for developing a large sulfide deposit. High resolution multiscale magnetics allows us to constrain the relative balance between periods of detachment faulting and magmatism to better describe accretionary processes on an ultraslow spreading ridge.

## Introduction

Accretion at mid-ocean ridges (MOR) has been documented to occur either in a symmetrical mode or asymmetrically<sup>1,2</sup>. Symmetrical accretion is most often dominated by magmatic processes, with high-angle normal faulting, and the formation of abyssal hills on both MOR flanks<sup>3</sup>. In contrast, asymmetric accretion, typically shows an interplay between weaker magmatic and tectonic processes that is typical of both slow and ultraslow spreading ridges<sup>1,4,5</sup>. The development of detachment faults (DFs), is the primary tectonic process that leads to thinning of the crustal section and the exposure of lower crust and ultramafic mantle material on corrugated fault surfaces<sup>6,7</sup>. Furthermore, these faults allow seawater to infiltrate deep into the footwall, that can result in enhanced hydrothermal circulation and the deposition of polymetallic sulfide<sup>8-10</sup>. Repeated fault movement also allows for the permeability in the hanging wall to be reactivated periodically, which could control both the longevity of a hydrothermal system and its activity through time<sup>11</sup>.

Research on the structure and evolution of DFs has mainly focused on slow spreading environments of the Mid-Atlantic Ridge (MAR) with only a few examples from ultraslow spreading environments such as the Southwest Indian Ocean Ridge (SWIR), and then only for areas that have little or no hydrothermal activity<sup>12,13</sup>. Few studies have investigated the detailed relationships between the evolution of DF systems and their associated hydrothermal systems at ultraslow spreading ridges mostly because it is difficult to accurately constrain the timing and because neovolcanic activity is broadly dispersed throughout the rift valley<sup>14</sup>.

In this study, we analyze a series of high-resolution magnetic surveys (Fig. 1b)<sup>15,16</sup> from the Dragon Horn area on the ultra-slow SWIR (49.7°E) where a deep-seated high-temperature hydrothermal circulation system has developed in close association with a major detachment faulting complex. Previous work has shown that the Dragon Horn DF system penetrates to almost  $13 \pm 2$  km depth below the seafloor and

hydrothermal fluids circulate almost 6 km deeper than the Moho boundary<sup>8</sup>. However, without a constraint on timing, it is still unclear how long a hydrothermal system with such a deep circulation geometry and heat source could be sustained and whether it would result in a large sulfide deposit<sup>17</sup>. Combining near-bottom magnetic data and newly available sea surface magnetic data with a large database of geological data (Fig. 1b), provides an opportunity to understand and finely constrain the geometry and evolution of an oceanic core complex (OCC) and its associated hydrothermal circulation system.

Our results at the Dragon Horn segment show that the older DF appears to have lasted approx. 0.72 My, and the present DF is likely only halfway through its evolution. The timeframe provides support for the hypothesis that hydrothermal circulation is mining heat over an extended period of time to support the development of a large sulfide deposit. High resolution multiscale magnetism allows us to better describe accretionary processes on an ultraslow spreading ridge and implies significant periods of accretionary hiatus.

## Results

**Sea surface magnetism and seafloor spreading framework.** The three sea-surface magnetic profiles (L1-L3, Fig. 2a) that have been reduced-to-the-pole (RTP), show the polarity structure of the ridge segment in a regional sense. The positive normal polarity Brunhes magnetic anomaly is found over the axial volcanic ridge (AVR) and rift valley, while a reverse polarity magnetic anomaly is generally found over the rift valley walls of both the north ridge flank and the southern flank that also encompasses the OCC dominated region. Through forward modeling we identify normal polarity Chrons C1n and C2An and the intervening reverse Chrons C1r/C2r on both MOR flanks – we note that Chron C2n is only poorly resolved in the sea surface profiles (Fig. 2). The boundaries of C1n and C2An match well with previous results<sup>18,19</sup>, and allow us to calculate the average half-spreading rates for each ridge flank for these intervals. Half-spreading rates for profiles L1, L2 and L3 (See Fig. 2c ~ 2e) are calculated from the middle of Chron C2An.1n (2.81 My) to the peak of the axial Brunhes anomaly (C1n, 0 My), which is assumed to be the time-averaged axis of spreading (and are noted as Vc1s or Vc1n - corresponding to the rates to the south and north). To the north, these half-spreading rates show small differences between the profiles ranging from 7.48 to 6.82 to 7.01 km/My (mean  $7.10 \pm 0.34$  km/My) for L1 through L3 respectively. To the south, however, there are more obvious changes in half-spreading rates varying from 7.08 to 7.97 to 8.43 km/My for profiles L1 through L3 respectively (mean  $7.83 \pm 0.69$  km/My). The total mean opening rate is 14.84 km/My for present day to Chron 2A, which is slightly faster than 13.89 km/My reported by ref.<sup>18</sup> for the period from Brunhes to Chron 3A. While all profiles show some asymmetry, profile L3 shows the greatest asymmetry in half-spreading rate with ~ 20% asymmetry relative to the north. In fact, the Brunhes polarity appears to extend to the south over the OCC2 on this profile, which we interpret as normal polarity crust that has been exhumed on the detachment fault and translated to the south. By comparing profile L3 with the undisturbed L1 profile, (Fig. 2e), we find about 3.8 km of additional extension on the detachment fault of profile L3.

**Detailed observations of the OCC2 detachment fault.** The high-resolution bathymetry (Supplementary Fig. 1) provides a good starting basis for understanding the evolution of the Dragon Horn detachment fault system, which displays features that include: a mullioned structure on the OCC2 fault surface, a clear breakaway trace (B2) and the distinct definition of its termination (T2). Sea surface magnetic profiles (Fig. 2) show that, in general, the south flank of the rift valley wall is within the reverse Matuyama polarity chron, with the exception of the Dragon Horn OCC2 itself, which, as noted earlier, has a small positive anomaly over it. The high-resolution near-bottom AUV magnetic RTP anomaly data (Fig. 3a) provide further detail on this magnetic character with negative magnetic anomalies on the lower slopes of the OCC2 and a slightly more positive magnetic anomaly over the top of a stranded hanging wall block on the fault surface and a stronger positive anomaly at just south of the breakaway (B2) summit. These positive anomalies in the near bottom data (Fig. 3), when continued upward to the sea surface, appear to produce the small positive anomaly on the side of the Brunhes anomaly of the sea surface profile L3 (Fig. 2). A zone of higher magnetic anomaly is also located at the western edge of the detachment fault on an apparent hanging wall block that hosts the LQ-1 vent field. Further off-axis, a zone of low magnetic anomaly is found associated with the termination of the older OCC1 in the southern part of the survey area (Fig. 3a).

The 3D focused magnetization inversion (Fig. 3c) provides another view of the crustal magnetization structure and how it relates to the DF and OCC structure. The focused magnetization result is decomposed into depth slices (Fig. 3c) and shows a weak magnetization over most of the OCC fault surface, a zone of positive magnetization associated with the top of the stranded block on the OCC2 surface and another zone of stronger positive magnetization along the south side of the breakaway B2. The range of strong magnetization intensity of the stranded block does not appear to decrease with depth, which likely means that there is indeed a relatively thick block along T2' that has detached from the initial breakaway at B2, where a zone of strong magnetization also exists (Fig. 3c). The talus zone at termination T2 at the base of OCC2, appears to show near zero magnetization values possibly indicating randomly oriented blocks compared to more coherently magnetized crust nearby.

The affect of hydrothermal activity on the magnetic signal at inactive vent site LQ-3 appears to be muted, however, by extracting the raw profile data (Fig. 3b) that crosses the vent site from east to west (marked by double arrow line in Fig. 3a) shows a narrow but obvious magnetic anomaly low over the vent site with about 200 m width (circled by red dotted line in Fig. 3b). Altered basalt was sampled from this site, inferring that focused hydrothermal alteration has only influenced the basaltic crust locally in the vicinity of LQ-3. Further west, active vent site LQ-1 is located on the hanging wall of OCC2<sup>8</sup> but surveys (See supplementary material) do not show any clear magnetic low associated with LQ-1<sup>15</sup> and simply shows a relatively weak magnetization throughout the area that does not vary much with depth – at least to 238 m (Supplementary Fig. 2d). One possible interpretation of this result suggests that there has been pervasive alteration in this region such that no large magnetization contrasts are present in the upper part of the crust.

**Rock samples and physical properties.** Rock samples collected with the Chinese TV grab document the lithologies present on the OCC fault surfaces and adjacent terrain (Supplementary Table 1, Fig. 4a and 4b). Basalt, gabbro and peridotite samples are variously distributed across the OCC1 surface and show the influence of processes such as amphibolization, chloritization and serpentinization. Specifically, as shown in Fig. 4a and 4b, ultramafic samples P1 – P4 are all located on or near the OCC2 surface. P1 and P2 were collected upslope from the LQ-1 vent site on the detachment fault surface, and the percentage of ultramafic rocks at P2, is higher and alteration more pervasive than at P1, presumably because P2 is nearer to the termination T2 and thus from deeper in the crustal section. P3 and P4 are located on the slip plane where the bend due to detachment tectonism and fracture caused by the decollement are documented in their deformation microstructure. Relatively fresh basalt and strongly altered peridotite are found at P5, which is probably the result of a talus accumulation at the base of the OCC slope from the collapsing section further up slope. The corresponding photomicrograph of P5 shows that the peridotite is strongly altered and contains magnetite. Samples from stations S1 – S4, near the LQ-3 vent site are basaltic rock that are heavily brecciated with different degrees of alteration. As noted earlier, the vent site LQ-3 likely enabled hydrothermal fluid to alter the surrounding host rock in this area. The basalt is heavily brecciated and contains quartz and opaque iron minerals and/or is filled with chlorite. Banded alteration haloes are ubiquitous in the samples suggesting pervasive hydrothermal alteration.

**Forward modeling of OCC profile.** To gain more detailed insight into the evolution of the OCC2 region we forward modeled the observed near-bottom magnetic anomaly by assuming typical values for the magnetization of the various lithologies and to more realistically account for changes in the direction of the magnetic vector as the detachment fault rotates and as magnetic polarity reversals occur as part of the MOR accretion process<sup>20</sup>. We selected profile PP' from the near bottom data (see Fig. 3a and 4a) and forward modeled the magnetic field to match the survey results by building a 2-D structural magnetic model using the method of Luo<sup>21</sup> (Fig. 5a and 5b).

In modeling the magnetic anomaly signal along the profile, we targeted the following parameters to match the observed anomaly: i) a magnetic contrast at the base and termination of the OCC between the exposed gabbro and peridotite and the basalts of the neovolcanic zone based on measurements of recovered samples (see Supplementary Table 1), ii) incorporation of the polarity structure from the sea surface magnetic spreading history (Fig. 2e), iii) addition of mass wasting bodies that appear to have affected the crust along the profile. After setting these parameters, we find that the forward result (grey line in Fig. 5a) fails to match the observed data at the south end of the profile, especially between 37.815°S ~ 37.83°S, even though we have included zones of mass wasting (i.e. zones of zero magnetization). However, we find a much better match (magenta line in Fig. 5a) once we consider adding in a positive magnetic zone between chrons C1n and C2An approximately 9 km from the AVR. This positive zone could be either be the short Jaramillo event (0.99–1.07 My) or possibly the older and slightly longer C2n chron (1.77–1.95 My). The C2n solution would imply very slow and then very fast spreading between the event and the Brunhes (1.76 km/My) and the event and the C2A chron (15.47 km/My) respectively, which seems improbable. The Jaramillo solution results in a more even

spreading rate between the event and the Brunhes and the event and the older C2A chron (7.6 km/My and 8.26 km/My respectively). Thus, we interpret this positive zone as most likely being Jaramillo in age. From the near bottom magnetic anomaly map (Fig. 3a), we find that this positive zone extends along strike to the east, at least as far as 49.69°E (Fig. 3a). It is not visible in the sea surface profile of L3 (Fig. 2e) at 49.72°E, although we see indication of an older anomaly that is likely chron C2n further south. Furthermore, using the distance between the Brunhes boundary and the present axis of spreading of 7.1 km, we estimate that the spreading half-rate that encompasses the OCC2 fault is 9.1 km/My, which is much faster than the subsequent accretionary spreading of 7.6 km/My from Brunhes to Jaramillo where the distance is ~ 1.9 km according to Fig. 6. The detachment fault slip thus may be accommodating more to the overall asymmetrical spreading in this ridge segment. This local asymmetry in spreading rate reaches up to 30% faster relative to the normal flank spreading rate, which is greater than any asymmetry seen at the MAR<sup>22</sup>.

## Discussion

**Evolution of the Dragon Horn detachment fault.** We have mapped the evolutionary history for a portion of the ridge flank based on the half spreading rates measured along magnetic profiles L2 and L3 and in the near bottom magnetic data. If we assume that OCC formation is initiated at the rift valley wall, typically located 3 to 6 km distant from the AVR accretionary axis (Fig. 6) and that OCC2 is still actively slipping, based on in situ observations, then we can reconstruct the history of OCC formation.

Starting with Profile L2, which has the best definition of both OCC1 and OCC2, we begin at the present day and restore the section sequentially through time. If we assume the present-day fault at OCC2 is active and continuing to slip as indicated by the seismic activity<sup>23</sup>, then we can restore the fault slip using the estimated half spreading rate of 7.97 km/My calculated earlier from the L2 profile (Fig. 2). The termination (T2) of OCC2 is located approximately 5.9 km from the present-day axis of spreading. Given the lateral slip distance on OCC2 of 2.6 km results in an initiation age of 0.33 My BP for OCC2 (Fig. 6a). There is approximately 3.4 km between the breakaway (B2) of OCC2 and the termination (T1) of the older OCC1. If we assume the older OCC1 formed at the same distance from the spreading axis as the present day OCC2 i.e. 5.9 km, this would translate into 0.43 My of spreading, suggesting that OCC1 (T1) stopped slipping approx. 0.76 My BP (i.e. 0.33 + 0.43 My). Restoring the slip on OCC1 of 5.7 km at 7.97 km/My gives a time duration of 0.72 My. Adding this time to the age at the end of slip on OCC1 gives an initiation time of 1.48 My BP for the formation of the OCC1 breakaway B2 (Fig. 6a).

Along profile L3, the older OCC1 is not well-defined, however, for the younger OCC2 we have noted that the Brunhes appears to be extended further here than the other profiles (Fig. 2), which is likely due to the formation of a stranded block (T2'-B2', with ~ 500 m width) on the surface of OCC2. As noted earlier we have also identified the Jaramillo event in the high resolution near bottom magnetic data (Fig. 5), which provides additional constraints on spreading half-rates. We estimated a half spreading rate of 7.6 km/My for the period between Jaramillo and the Brunhes chron, but a faster 9.1 km/My for the Brunhes chron to the AVR, which encompasses the OCC2 fault. If we use the fast spreading half rate of 9.1 km/My for the

slip on OCC2, again assuming it is currently active, we get a period of time of 0.31 My, slightly shorter than the estimate from profile L2 (Fig. 6b). If the fault initiated 0.31 My BP then there would have been 0.47 My of previous crustal spreading to create the Brunhes chron, which at the 9.1 km/My rate would have resulted in 4.3 km of crustal accretion. Given that the fault termination (T2) is located 3.5 km from the axis (AVR) and adds the width of stranded block, then the fault clearly initiated within the normal polarity Brunhes chron, about 300 m from the Brunhes/Matuyama boundary. This is consistent with the observation that the present-day fault breakaway (B2) is ~ 300 m within the Brunhes chron (Fig. 5a). As noted in Fig. 1, Profile L3 does not have a clear expression of OCC1, which is present further west on Profile L2. Calculations from L2 suggest OCC1 initiated 1.48 My BP and terminated at 0.76 My BP, which would have obviated the accretion of Jaramillo-aged crust if all the extension was taken up by slip on OCC1 along profile L2.

If we assume the periods when the OCCs were actively slipping were times of reduced magmatic supply, our evolutionary history for the Dragon Horn segment would imply that magmatic episodes of spreading occurred between 2.8 My and 1.48 My BP and again between 0.76 My and 0.33 My BP. Similarly, slip on the old detachment fault (OCC1) appears to have lasted approx. 0.72 My, which is within previous estimates of DF slip in other SWIR segments 0.6 to 1.5 My.<sup>24</sup> The young DF of OCC2 has been active for ~ 0.33 My and may continue for another ~ 0.4 My if the evolution time of DF1 is considered representative of a complete cycle.

**Detachment faulting system and control on hydrothermal activity.** We believe that the most recent OCC2 at the Dragon Horn segment formed in two main steps (Fig. 6c). The original detachment fault DF2 formed at the breakaway B2 (0.31 ~ 0.33 My BP) and originally stopped at termination T2'. Sometime afterwards, the main slip on the detachment fault stepped further to the south and initiated a second breakaway B2' on a slip plane that strands a block (T2' - B2') on the surface of the scarp face. The stranded block correlates with a modestly high magnetic anomaly along the middle of the detachment surface. This block used to form part of the hanging wall but is now a stranded footwall block. The upper portion of the OCC2 surface, above T2', is the fossil footwall, while the lower section of the OCC2 slip surface B2' to T2 is now the exposed active fault (Fig. 6c).

The inactive LQ-3 hydrothermal vent field, located on top of this stranded block on the mid-slope bench between B2' and T2' and was likely active following the detachment fault began to initiate at B2 that is 0.33 My Bp, and may have become inactive as it was stranded on its block and became separated from its fluid circulation system and heat source. If we assume continuous slip on the OCC2 and partition time between the old and present-day slip surfaces simply based on the lateral distance, then we can estimate when LQ-3 might have stopped venting. The inactive fault surface (B2-T2') is ~ 0.4 km wide. Using the interval half spreading rate of 9.1 km/My this would translate into the current slip occurring ~ 46 kyr when the main OCC detachment jumped from its previous location to its present location and formed the stranded block. We speculate that the LQ-3 vent site was actively venting up to 46 kyr prior to the faulting event that formed the stranded block and since that time the vent site has become inactive.

At the western edge of OCC2, the stranded block discussed above causes a lateral offset in the trace of the termination T2 (Fig. 4a). This offset in the trace of the termination means that the active fault surface of OCC2 is revealed upslope as a disconnected portion of the termination T2 at this western edge. Just down slope from T2 is the hanging block that hosts the LQ-1 vent field (Fig. 4a). The LQ-1 vent field includes the M and S zones, with the M zone probably being younger than the S zone. *HOV Jiaolong* investigations show that there are more inactive vents in the S zone compared with the M zone, and that the temperature of active vents in S are generally lower than those in M zone (Supplementary Fig. 3). The distribution of vent zones suggests a progressive migration of activity along a hydrothermal channel or fault zone<sup>25</sup> from the S zone to the M zone.

We speculate that the LQ-1 vent field may have formed at the same time as the LQ-3 vent site. It may have become inactive after the LQ-3 stranded block formed, but then came back to life more recently as activity is now ongoing. This speculation is supported by detailed mineralogical patterns found in the chimneys and dating of the sulfides. A relict chimney collected from the M zone shows abundant medium grained chalcopyrite forms granular aggregates around the inner channels and fine- to medium-grained pyrite and sphalerite to be intergrown with minor chalcopyrite around the outer part of the chimney<sup>26</sup>. This indicates that the chimney had a low temperature environment early in its formation as an outer pyrite-rich layer formed followed by a period of high temperature that formed the inner chalcopyrite-rich lining. We speculate that hydrothermal venting at LQ-1, although located on a hanging wall block, maybe linked to this stranded block formation. For this case, the faulting activity forming the stranded block has apparently led to a rejuvenation of the thermal pathways for fluid flow and enhanced fluid discharge through the hanging wall block. Furthermore, as discussed earlier, if we assume the DF2 system may continue to be active for another 0.4 My and allow hydrothermal circulation to tap heat over an extended period this would suggest that LQ-1 may continue to grow as a large sulfide deposit.

Additional hydrothermal activity appears to have occurred continuously during the evolution of the DF system inferring that the inactive LJ-E vent field may have been active sometime during 0.76–1.48 My BP when DF1 was active. The LJ-W hydrothermal anomaly was investigated<sup>27</sup> but no vent has been detected. We suggest that because heat is mainly being mined by the hydrothermal system related to the younger DF2 system, only a small amount of hydrothermal activity is focused through the path of the older DF1 system to the LJ-W site.

**Intermittent detachment faulting and episodic magmatic accretion.** High resolution multiscale magnetism allows us to constrain the relative balance between periods of detachment faulting and magmatism to better describe accretionary processes on an ultraslow spreading ridge. We find that detachment fault OCC2 initiated 5.9 km from the AVR on profile L2 and has been slipping on the fault for the past 0.33 My during which no appreciable magmatic accretion has occurred. The 3.4 km of accreted crust between OCC2 and the previous OCC1 represents 0.43 My of accretion between 0.33 My and 0.76 My after OCC1 stopped slipping. We have hypothesized that the old OCC1 formed at the same distance from the AVR as the present day OCC2, i.e, 5.9 km, which given the 5.7 km of slip on OCC1 means that OCC1 initiated 1.48 My BP. Again, we assert that no appreciable magmatic accretion occurred during the period between 0.76

MyBP and 1.48 MyBP. This magmatic episodicity linked with the record of fault initiation and slip means that the accretionary record will have significant hiatuses with respect to distance from the AVR. As shown in Fig. 6a, the age of crust between OCC1 and OCC2 i.e. B2 and T1 is 1.79 to 2.22 My, while the crust between the AVR and OCC2 (T2 termination) is highly affected with ages of 0-0.33, 0.33 to 0.76 and 1.48 to 1.79 My. Ref.<sup>14</sup> has proposed the similar viewpoint according to U-series eruption ages of volcanic rocks collected from SWIR (11°–15°E), whereas our study shows that we can constrain these processes based on a detailed magnetic framework for detachment faulting systems on an ultraslow-spreading ridge. Multi-scale magnetic surveys are a useful approach for constructing a framework to accurately describe the timing of magmatic and tectonic processes involved in the crustal accretion at ultraslow-spreading ridges.

## Methods

**Sea-surface magnetic survey.** Sea surface magnetic mapping during recent Chinese cruises collected additional profiles over the Dragon Horn ridge segment<sup>30</sup>. We processed these Chinese magnetic profiles by removing the International Geomagnetic Reference Field (IGRF)<sup>31</sup> and phase-shifting the anomaly profiles using a reduced-to-the-pole (RTP) transformation assuming a geocentric axial dipole (GAD) for the area (i.e. inclination of -62.3° and a declination of -42°) (Fig. 2). We note that the easternmost survey line L1 appears to be unaffected by the Dragon Horn detachment fault system and so we can use it as a reference anomaly sequence for the area (Fig. 3). We carried out 2-D forward modeling to identify the magnetic anomalies using the geomagnetic polarity timescale.<sup>32</sup> (Fig. 3). We assumed a constant 1000 m thick magnetic layer with the upper surface defined by the bathymetry with a 9 A/m magnetization for the Brunhes period (0-0.78 My) and a uniform  $\pm 6$  A/m magnetization for the off-axis crust. The effect of sloped polarity boundaries on magnetic anomaly amplitude has been ignored in the modeling.

**Near-bottom magnetic survey.** The first near-bottom magnetic data of the Dragon Horn area were collected by AUV *ABE* in 2007<sup>15</sup> followed by a Chinese sea surface magnetic survey in 2008<sup>30</sup>. Several Chinese research cruises visited the area more recently and have collected additional near-bottom magnetic data as part of a broader effort to document the nature and distribution of OCCs and hydrothermal systems of this region<sup>33</sup>. Between 2015 and 2018, seven AUV *Qianlong II* dives (AUV022–026, AUV048 and AUV050) were conducted in the Dragon Horn area during cruises DY40 and DY49 on board R/V *Xiangyanghong 10* (Fig. 1b). Magnetic data were collected with 1 Hz sampling frequency, using a tri-axial fluxgate magnetometer installed on the stern of the AUV *Qianlong II*<sup>16</sup>. In general, the AUV operated at approximately 100 m above the seafloor with a nominal track spacing of 400 m and an average transit speed of 1 m/s. High-resolution bathymetry and hydrothermal plume mapping data were collected concurrently during these surveys. Rock samples were obtained separately by the Chinese TV grab at locations marked in Fig. 1b.

AUV048 traversed over the LJ-W field and AUV050 made just one crossing of the LJ-E vent field and both were confined to traversing over the oldest terrain of the study area (OCC1). Therefore, we have primarily analyzed the near-bottom magnetic data over the youngest part of the terrain that includes OCC2 and its associated vent fields using five of seven AUV dives (AUV022–026). In addition to the magnetic analysis, we also measured the physical, geochemical and microstructural properties of rock samples collected by the Chinese TV grab to help in the interpretation of the near-bottom magnetic anomalies. The study area includes all of the detected hydrothermal sites found by the HOV *Jiaolong*, the area surveyed by three of the *ABE* dives (ABE200–202) plus the multi-stage detachment OCC2 breakaway and termination region on the south flank of the Dragon Horn segment (Fig. 2). We reanalyzed the magnetic data from *ABE* dive 201 because it was surveyed at 50 m altitude and at a track spacing of 30 m, and thus provides a higher resolution dataset than the AUV *Qianlong II* surveys and can now be placed in better context with the broader mapping results.

Analysis of the AUV *Qianlong II* magnetic data included calibration and correction of the data for the magnetic effects of the vehicle and this was accomplished by spinning the AUV at the beginning of the dive once it had reached its operating depth. A five-factor trigonometric function method is used to calculate the calibration coefficients that are then applied to the measured magnetic data<sup>34</sup>. In order to account for any diurnal variations during the near-bottom magnetic surveys, a seafloor magnetometer was moored at a stationary location as a temporary geomagnetic station<sup>16</sup>. These diurnal variations were removed from the measured magnetic field followed by correction for the IGRF. We then applied filtering with a seven-second moving average filter (about 7 m averaging) to smooth the resultant magnetic anomaly data<sup>25</sup>. These AUV data were gridded with a minimum curvature method and RTP by assuming that the magnetization direction is parallel to the GAD for the area, as noted earlier (Fig. 3a). The influence of the fluctuating depth of the AUV survey lines was ignored for this RTP transformation. However, terrain undulation was considered in the further post processing inversion steps.

We used a 3-D focused inversion method to invert for a 3-D magnetization distribution with depth (Fig. 3c)<sup>35</sup>. This focused inversion process adds a terrain-weighting matrix to overcome the effect of undulating terrain on the inversion results. A depth-weighting function and a minimum support function are also employed to counteract the natural decay of the potential field with distance and to avoid singularities respectively<sup>36</sup>. For these inversions, we assumed GAD directions for the geomagnetic field and magnetization.

## Declarations

**Data availability.** Sea surface magnetic profiles, near bottom magnetic grids, altitude and bathymetry can be requested from the corresponding author Chuanhui Tao (taochunhuimail@163.com). The lithologic characters and magnetization of samples in Dragon Horn collected by TV grab supplied in the Supplementary Tables.

## Acknowledgement

We thank Science Party, captains and crew of COMRA Cruise DY19<sup>th</sup>, DY40<sup>th</sup> and DY49<sup>th</sup>, the 4,500 m Qianlong-II Autonomous Underwater Vehicle team and the submersible *Jiaolong* group. This work was supported by National Key R&D Program of China under contract NO. 2018YFC0309901, National Natural Science Foundation of China (41906065), National Key R&D Program of China (2017YFC0306803) and COMRA Major Project under contract No. DY135-S1-01-06 and No. DY135-S1-01-01.

### Author contributions

T.W. carried out the investigation and the analysis, and wrote the manuscript. M.T. contributed to the analysis and the writing. C.H. T. conceived of the project and contributed the interpretation and writing. J.H. Z. participated in the investigation. F. Z. supplied the 3D focused inversion method. Y.L. L. participated in the interpretation of the results. All authors participated in the review of this manuscript.

### Data availability

Sea surface magnetic profiles, near bottom magnetic grids, altitude and bathymetry would supply in the related website. The lithologic characters and magnetization of samples in Dragon Horn collected by TV grab supplied in the Supplementary Tables.

### Additional information

Supplementary Information accompanies this paper at <http://www.nature.com/naturecommunications>

**Competing financial interests:** The authors declare no competing financial interests.

**Reprints and permission** information is available online at <http://npg.nature.com/reprintsandpermissions/>

## References

1. Escartín, J. et al. Central role of detachment faults in accretion of slow-spreading oceanic lithosphere. *Nature*. **455**, 790-794 (2008).
2. Smith, D. K. Fault rotation and core complex formation: Significant processes in seafloor formation at slow-spreading mid-ocean ridges (Mid-Atlantic Ridge, 13°–15°N). *Geophy. Geosy.* **9**, n/a-n/a (2008).
3. Buck, W. R., Lavier, L. L. & Poliakov, A. N. B. Modes of faulting at mid-ocean ridges. *Nature*. **434**, 719-723 (2005).
4. Simon, A., Javier, E. U. E. & Searle, R. C. Extremely asymmetric magmatic accretion of oceanic crust at the ends of slow-spreading ridge segments. *Geology* **28**, 179-182 (2000).
5. Wijk, J. W. V. & Blackman, D. K. Deformation of oceanic lithosphere near slow-spreading ridge discontinuities. *Tectonophysics*. **407**, 211-225 (2005).

6. Cann, J. R. et al. Corrugated slip surfaces formed at ridge-transform intersections on the Mid-Atlantic Ridge. *Nature*. **385**, 329-332 (1997).
7. MacLeod, C. J., et al., Life cycle of oceanic core complexes, *Planet. Sc. Lett.* **287**, 333–344 (2009).
8. Tao, C. et al. Deep high-temperature hydrothermal circulation in a detachment faulting system on the ultra-slow spreading ridge. *Commun.* **11**, 1300 (2020).
9. Mccaig, A. M., Cliff, R. A., Escartin, J., Fallick, A. E. & Macleod, C. J. Oceanic detachment faults focus very large volumes of black smoker fluids. *Geology*. **35**, 935-938 (2007).
10. Fouquet, Y., et al., Geodiversity of hydrothermal processes along the Mid-Atlantic Ridge and ultramafic-hosted mineralization: a new type of oceanic Cu-Zn-Co-Au volcanogenic massive sulfide deposit, Diversity of hydrothermal systems on slow spreading ocean ridges. AGU Geophys. Monograph Series **188**, 321–367 (2013).
11. Tivey, M. A., H. Schouten & M. C. Kleinrock, A near-bottom magnetic survey of the Mid-Atlantic Ridge axis at 26°N: Implications for the tectonic evolution of the TAG segment. *Geophys. Res.* **108**, 2277 (2003).
12. Cannat, M., et al., Modes of seafloor generation at a melt-poor ultraslow-spreading ridge, *Geology* **34**, 605-608 (2006).
13. Sauter, D. et al., Continuous exhumation of mantle-derived rocks at the Southwest Indian Ridge for 11 million years. *Geosci.* **6**, 314-320 (2013).
14. Standish, J. J. & Sims, K. W. W., Young off-axis volcanism along the ultraslow-spreading Southwest Indian Ridge. *Geosci.* **3**, 286-292 (2010).
15. Zhu, J. et al. A reduced crustal magnetization zone near the first observed active hydrothermal vent field on the Southwest Indian Ridge. *Res. Lett.* **37**, n/a-n/a (2010).
16. Wu, T. et al. A hydrothermal investigation system for the Qianlong-II autonomous underwater vehicle. *Acta Oceanol. Sin.* **38**, 159-165 (2019).
17. Hannington, M.D., Jamieson, J., Monecke, T., & Petersen, S., Modern seafloor massive sulfides and base metal resources: Towards an estimate of global seafloor massive sulfide potential: Society of Economic Geologists Special Publication **15**, 317–338 (2010).
18. Mendel, V. et al. Magmato-Tectonic Cyclicity at the Ultra-Slow Spreading Southwest Indian Ridge: Evidence from Variations of Axial Volcanic Ridge Morphology and Abyssal Hills Pattern. *Geophys. Geosy.* **4**, n/a-n/a (2003).
19. Sauter, D., et al., Ridge segmentation and the magnetic structure of the Southwest Indian Ridge (at 50 30' E, 55 30' E and 66 20' E): Implications for magmatic processes at ultraslow-spreading centers. *Geophys. Geosy.* **5**, n/a-n/a (2004).
20. Reston, T. J. & Ranero, C. R. The 3-D geometry of detachment faulting at mid-ocean ridges. *Geophys. Geosy.* **12**, n/a-n/a (2011).
21. Luo, Y. & C. L. Yao. Theoretical study on cuboid magnetic field and its gradient expression without analytic singular point. *Oil Geophysical Prospecting (in Chinese)* **42**, 714–19 (2007).

22. Mallows, C. & Searle, R. C. A geophysical study of oceanic core complexes and surrounding terrain, Mid-Atlantic Ridge 13°N–14°N. *Geophys. Geosy.* **13**, (2013).
23. Liu, Y. et al. Seismic activity recorded by a single OBS/H near the active Longqi hydrothermal vent at the ultraslow spreading Southwest Indian Ridge (49°39' E). *Georesour. Geotec.* **37**, 201-211 (2018).
24. Cannat, M. et al. On spreading modes and magma supply at slow and ultraslow mid-ocean ridges. *Earth Planet. Sc. Lett.* **519**, 223-233 (2019).
25. Tao, C., Wu, T., Liu, C., Li, H. & Zhang, J. Fault inference and boundary recognition based on near-bottom magnetic data in the Longqi hydrothermal field. *Geophys. Res.***38**, 17-25 (2016).
26. Liang, J., Tao, C., Yang, W., Liao, S. & Huang, W. 230Th/238U Dating of Sulfide Chimneys in the Longqi-1 Hydrothermal Field, Southwest Indian Ridge. *Bulletin of the Geological Society of China* **93(S2)**, 77-78 (2010).
27. Liao, S. et al. Surface sediment geochemistry and hydrothermal activity indicators in the Dragon Horn area on the Southwest Indian Ridge. *Geol.* **398**, 22-34 (2018).
28. Tucholke, B. E., Behn, M. D., Buck, W. R. & Lin, J. Role of melt supply in oceanic detachment faulting and formation of megamullions. *Geology.* **36**, 455–458 (2008).
29. Dick, H. J. B., Lin, J. & Schouten, H. An ultraslow-spreading class of ocean ridge. *Nature.* **426**, 405-412 (2003).
30. Zhang, T., Lin, J., & Gao, J. Y. Magmatism and tectonic processes in area a hydrothermal vent on the southwest indian ridge. *China.* **56(12)**, 2186-2197 (2013).
31. Finlay, C. C., et al., International Geomagnetic Reference Field: the eleventh generation. *J. Int.* **183(3)**, 1216-1230 (2003).
32. Cande, S. C. & Kent, D. V. Revised calibration of the geomagnetic polarity timescale for the Late Cretaceous and Cenozoic. *Geophys. Res. Solid Earth.* **100**, 6093-6095 (1995).
33. Tao, W., Tao, C., Tivey, M., & Jinhui, Z., High-resolution magnetic exploration of Longqi hydrothermal field (49.6° E) on SWIR (Abstract). AGU Fall Meeting, Washington DC (2018).
34. Tao, W., Chunhui, T., Jinhui, Z. & Cai, L. Correction of tri-axial magnetometer interference caused by an autonomous underwater vehicle near-bottom platform. *Eng.* **160**, 68-77 (2018).
35. Zhou, F., Tao, C., Wu, T., Zeng, Z. & Liu, C. 3D Focused Inversion of Near-bottom Magnetic Data from Autonomous Underwater Vehicle in Rough Seas. *Sci. J.* **53**, 405-412 (2018).
36. Okuma, S., Nakatsuka, T. & Ishizuka, Y. Aeromagnetic constraints on the subsurface structure of Usu Volcano, Hokkaido, Japan. *geophys.* **45**, 24-36 (2014).

## Figures

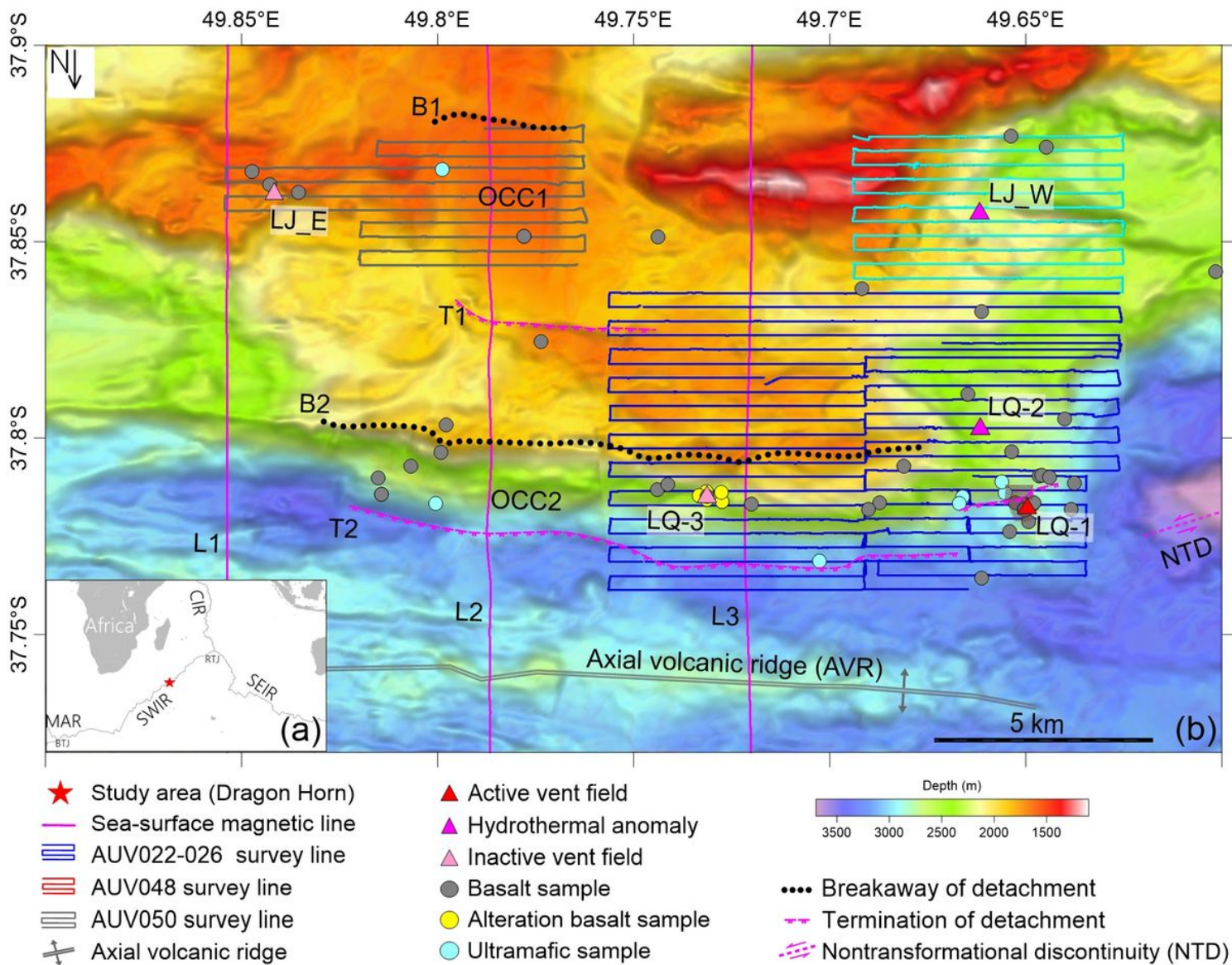


**Figure 1**

Bathymetry and geological settings of the Dragon Horn area segment 28 on the South West Indian Ridge (SWIR). (a). Regional location of the Dragon Horn area on the SWIR. (b) Summary bathymetry map with the distribution of hydrothermal fields (triangle markers) and geological tectonic features (Black dots are the locus of the DF breakaways, magenta hachured lines are the DF terminations, NTD is the non-transform discontinuity with segment 29). Sea surface magnetic survey lines (L1, L2, L3) that cross the Dragon Horn area are shown by magenta lines. AUV tracks are shown by pectinate lines.

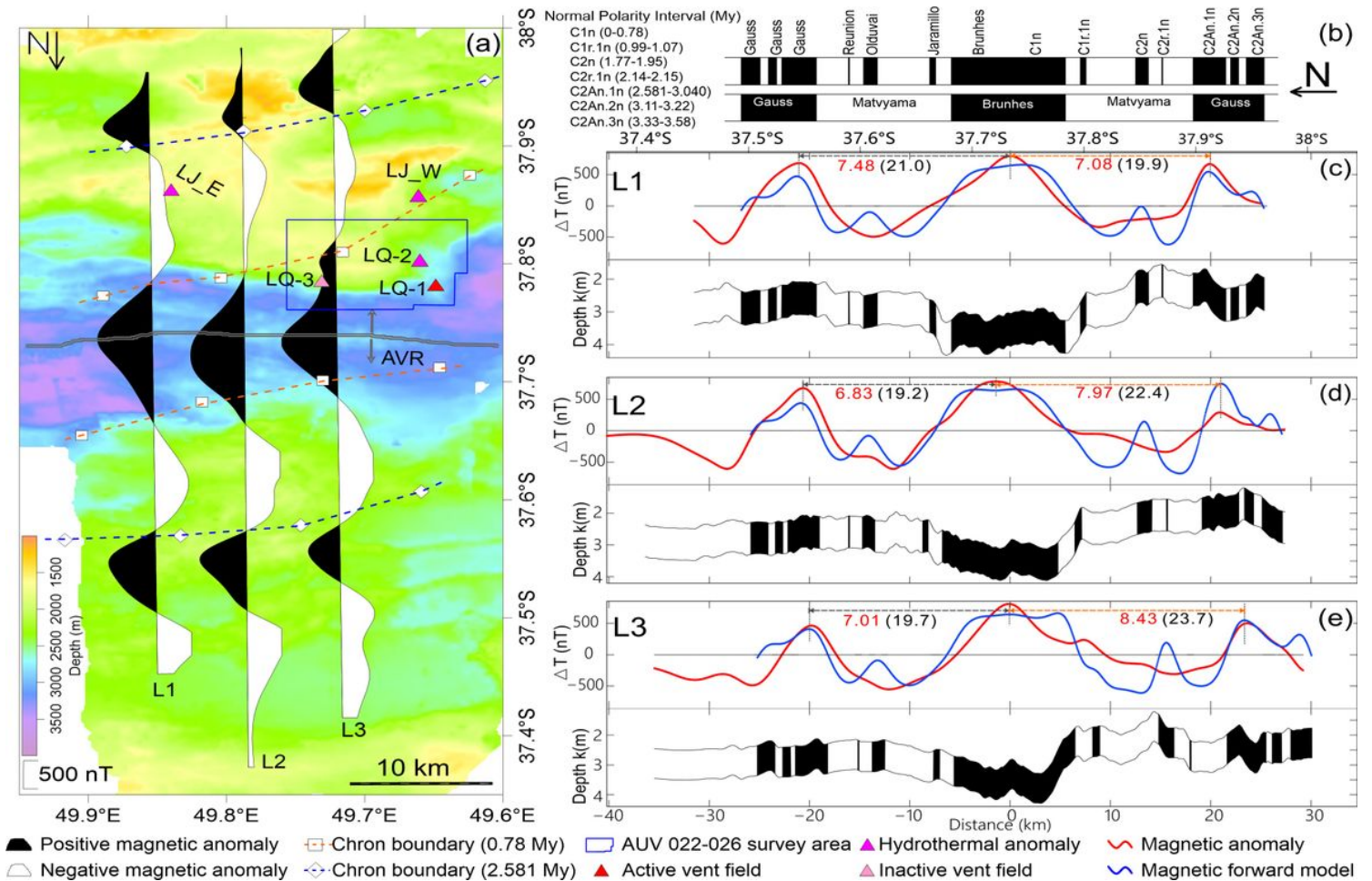


**Figure 2**

The regional magnetic polarity structure of the Dragon Horn ridge segment as documented by sea-surface magnetic survey profiles. (a) Magnetic anomaly lineations. The boundaries of Brunhes (0.78 My) and Matuyama (2.581 My) obtained by Sauter et al. [2004] are marked by dashes. (b) Geomagnetic polarity time scale [Cande and Kent, 1995]. (c), (d) and (e) are comparisons between magnetic forward modeling results and observed anomaly of profiles L1, L2 and L3 respectively, and their corresponding forward models assuming a constant thickness source layer with 1 km. Where the figures in (c), (d) and (e) noted by red color are half-spreading rates (in km/My) from the middle C2An.1n Chron to present-day are noted as Vc1n on the north flank and Vc1s on the south flank and black numbers are the corresponding distances (in km).

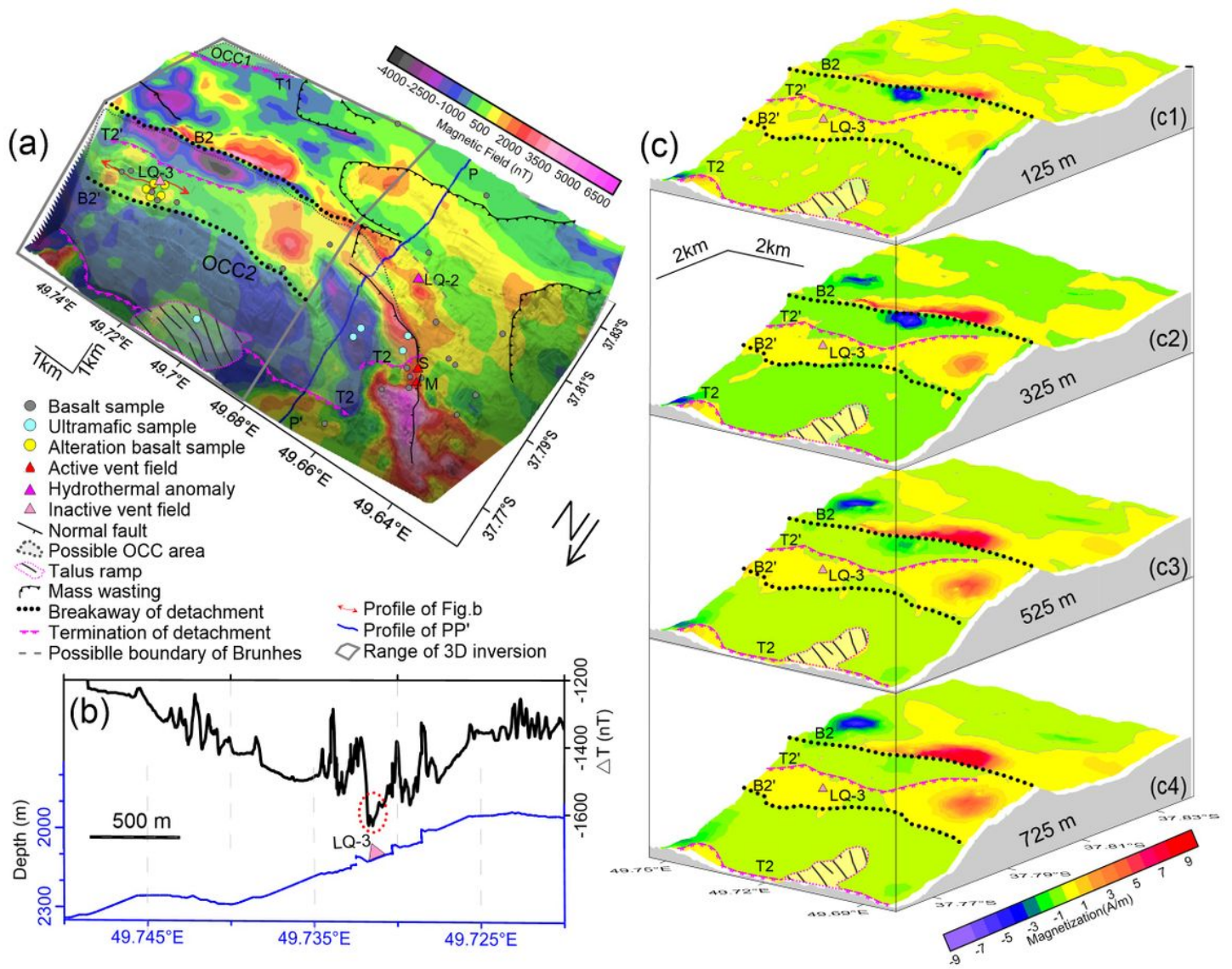


**Figure 3**

Near-bottom magnetic anomalies (a) and (b), and results of magnetization inversion (c) of the Dragon Horn OCC1 area. Specifically, (b) magnetic profile of a survey line which crosses vent field LQ-3 (marked by Double arrow line in (a)). (c) Focused 3-D magnetization inversion structure of the OCC1 system with (c1), (c2), (c3) and (c4) as the magnetization inversion results at depths 125 m, 325 m, 525 m and 725 m, respectively. We assume that the magnetization direction is parallel to the geocentric axial dipole (GAD, the geomagnetic inclination and declination with  $-62.3^\circ$  and  $-42.0^\circ$ , respectively).

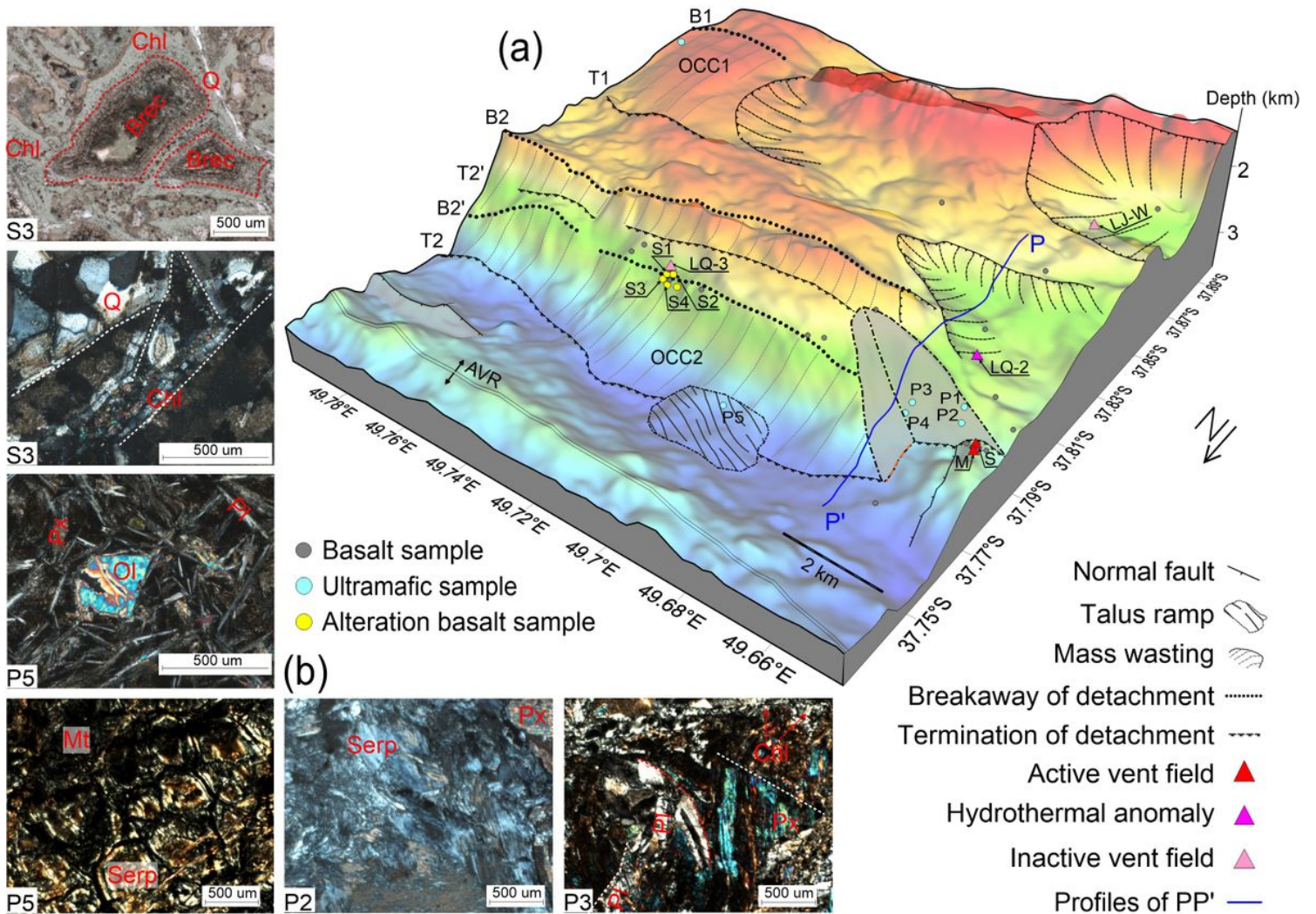


**Figure 4**

Interpretation of microphysiography of the Dragon Horn OCC2 system. (a) The basic geologic and morphologic structure. DF breakaways (B1, B2, B2') are shown by black dotted lines. DF terminations (T1, T2, T2') are shown by black hachured dashed lines. Thinner black hachured lines shown areas of mass wasting and trajectories of collapse. Grey shaded areas shows the edge of OCC2 fault surface near LQ-1. Lined area is a region of talus accumulated at the base of the OCC2 scarp. Triangle symbols are hydrothermal vent locations as described in the legend. Dots are sample locations with lithologies as described in Figure 1 caption. Blue line is Profile PP' modeled in Figure 5. (b) Photomicrograph and major minerals of representative rock samples which are observed in cross-polarized light, except the first (S3) with plane-polarized light. Sample S3, Altered basalt filled with chlorite and a small amount of quartz (Q) in the ring banded structure and basalt detritus. Sample P5, peridotite is strongly altered and has formed serpentine and magnetite (Mt). Sample P2 has a network structure and mainly contains serpentine (Serp), residual peridotite and pyroxenes (Px). Sample P3, bends and fractures are found and plagioclase (Pl), chlorite (Chl) and pyroxenes are present. Where the white dotted line is a fracture, red dotted curve line is a bend, and red enclosed line is a ring banded structure.

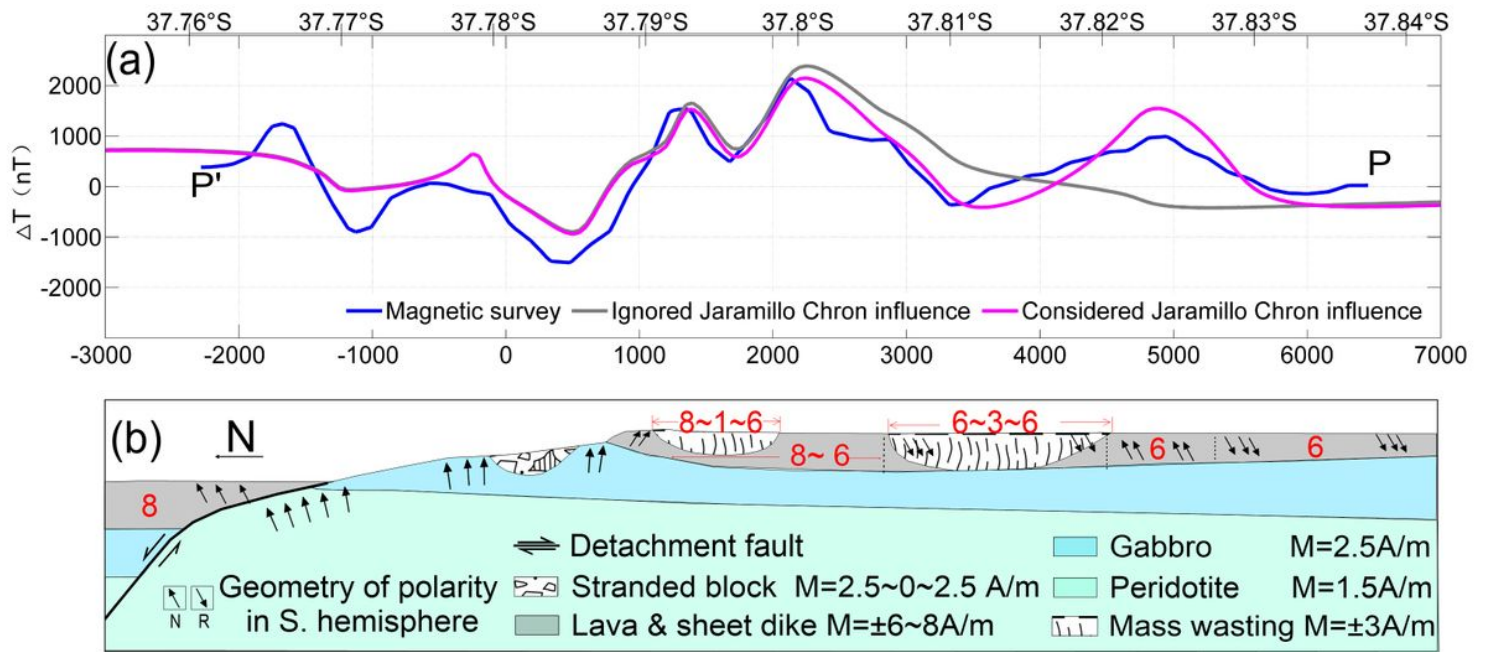


**Figure 5**

A comparison of forward magnetic modeling results (a) based on 2-D magnetic models shown in (b) with the observed magnetic profile PP' shown in bold blue line. We assumed that the angle of footwall rotated is linearly increasing with the distance to breakaway and the effective thickness of magnetic layer is 1 km. The figures noted by red color are the given magnetizations (in A/m) and the reversed magnetization corresponding to its negative values. The distance is about 4 km from the center X (value of 0) where is also approx. the center of OCC2.

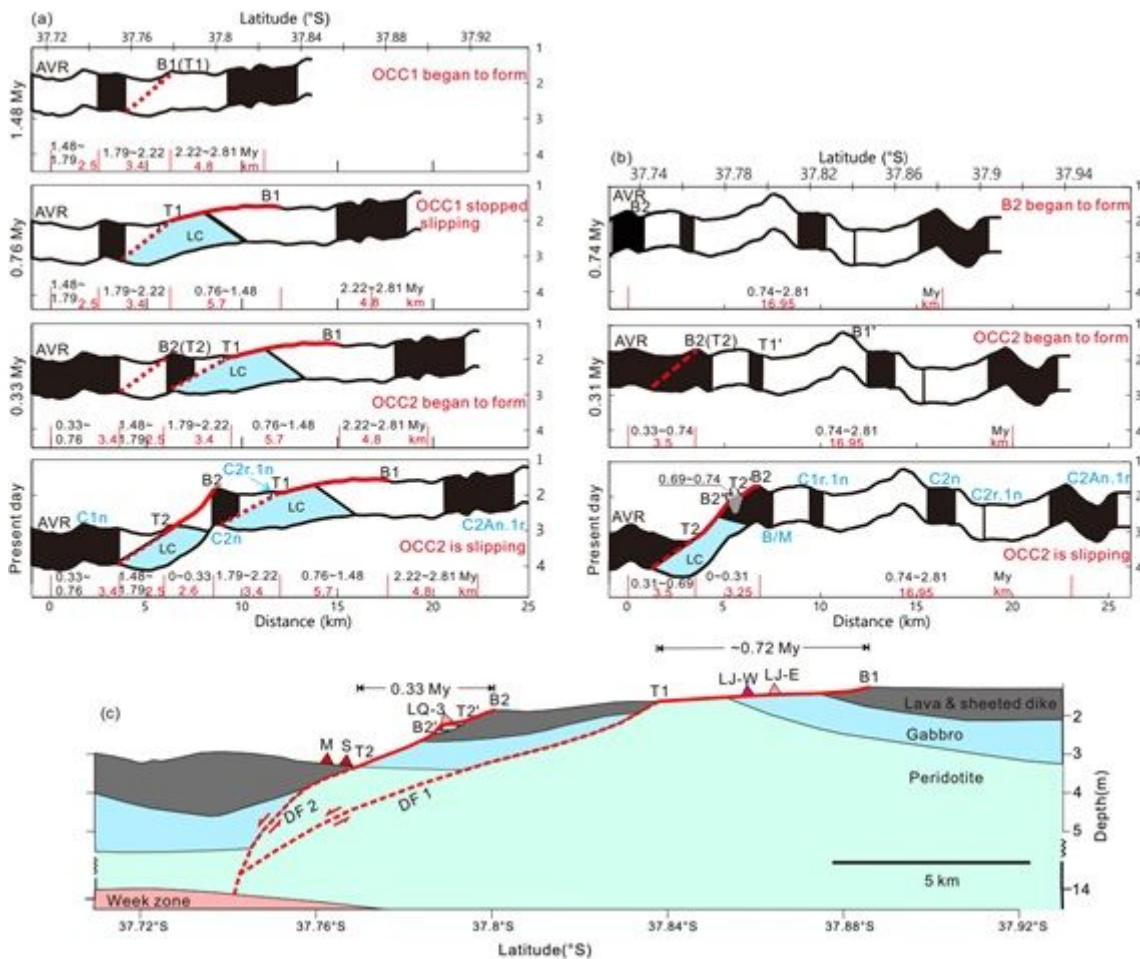


**Figure 6**

The evolutionary history of the detachment faulting system with hydrothermal activity based on profiles L2 and L3. Only upper crustal section is shown with corresponding spreading rate along profiles and projected polarity zones. AVR is the axial volcanic ridge and presumed zero age. a) Profile L2 evolution shown from 1.48 My BP to present and b) Profile L3 evolution shown from 0.74 My BP to present. Also shown are the breakaway B1 and termination T1 of OCC1 and the breakaway B2 and termination T2 of OCC2. Red lines represent the OCC slip surfaces, other lines are accretionary terrain, and grey area represents the stranded block on OCC2. LC refers to lower crust exhumed by OCC1 and OCC2 and presumed to be less magnetic than the upper crustal extrusive section. Slip is assumed to be continuous along the OCC fault surfaces when they are formed until they terminate (i.e. no stop and start behavior). OCCs are assumed to nucleate off axis approx. 3 to 6 km from the axis of spreading (NVZ). Topography is only approximate and may not reflect past topographic nature. c) present-day cross section of L2 profile showing the geometry of the detachment faults (red dashed lines) as determined by seismic data<sup>23</sup> and surface expression of the faults shown by red solid lines along with the inferred crustal units. The location of vent sites have been projected onto the cross-section.

## Supplementary Files

This is a list of supplementary files associated with this preprint. Click to download.

- [Supplementary.docx](#)
- [SupFig1.jpg](#)
- [SupFig2.jpg](#)
- [SupFig3.jpg](#)